



Multiwavelength Analysis and the Difference in the Behavior of the Spectral Features during the 2010 and 2014 Flaring Periods of the Blazar 3C 454.3

Raúl A. Amaya-Almazán¹ , Vahram Chavushyan¹ , and Victor M. Patiño-Álvarez^{1,2}

¹ Instituto Nacional de Astrofísica, Óptica y Electrónica, Luis Enrique Erro #1, Tonantzintla, Puebla 72840, Mexico; antonioaa@inaoep.mx, amayaalmazanra@gmail.com

² Max-Planck-Institut für Radioastronomie, Auf dem Hügel 69, D-53121 Bonn, Germany

Received 2020 April 17; revised 2020 October 15; accepted 2020 October 23; published 2020 December 29

Abstract

Over the years, the flat-spectrum radio quasar 3C 454.3 has presented phases of very high activity (flares) in which the different wave bands increase their flux dramatically. In this work, we perform multiwavelength analysis from radio to gamma-rays and study the Mg II $\lambda 2798$ emission line and the UV Fe II band from 2008 to 2018. We found that an increase in the 43 GHz flux density of the quasi-stationary component C coincides with the estimated time at which a superluminal blob ejected from the radio core (which caused the brightest flare of 2010) collides with the quasi-stationary component (at a projected distance of ~ 4.6 pc from the radio core). The different behavior of the spectral index in the first ($5000 < \text{JD} - 2,450,000 < 5600$) and second ($6600 < \text{JD} - 2,450,000 < 7900$) flaring periods suggests changes in the physical conditions. The complex nature of the second period can be a result of a superposition of multiple events at different locations. The Mg II line has an anticorrelation with the UV continuum while Fe II correlates positively, except at the time of the brightest flare of 2010, when both have a strong response at high continuum luminosities. Our results suggest that the dominant gamma-ray emission mechanism for the first flaring period is external Compton. For the second flaring period the region emitting seed photons is co-spatial with that emitting gamma-rays. However, a study of the spectral energy distribution using a multizone jet emission model is required to confirm the nature of each significant flare during the second period.

Unified Astronomy Thesaurus concepts: Active galaxies (17); Galaxy jets (601); Gamma-rays (637); Emission line galaxies (459); Quasars (1319); Active galactic nuclei (16)

Supporting material: figure sets, machine-readable table

1. Introduction

Flat-spectrum radio quasars (FSRQs), a subclass of blazar-type active galactic nuclei (AGNs), display key characteristics of blazars and quasars, very high variability, and emission lines. They display variability on a wide range of timescales (Fan et al. 2018; Gupta 2018) as well. In most FSRQs, the continuum from radio to UV is often dominated by nonthermal emission, which comes from a jet of relativistic plasma. The jet points along our line of sight (Urry & Padovani 1995) causing Doppler boosting (Sher 1968). The spectral energy distribution (SED) of this type of object has two main components. The low-energy component is mostly due to synchrotron emission and the high-energy component is due to inverse Compton (IC) scattering (e.g., Böttcher 2007; Böttcher et al. 2013; Romero et al. 2017). The process of emission through IC can be due to two different physical interactions in the central engine; one of these is called synchrotron self-Compton (SSC, Bloom & Marscher 1996), in which the seed photons, to be taken to higher energies by the relativistic electrons, come from the synchrotron emission produced in the jet itself. On the other hand, in external inverse Compton (EC, Sikora et al. 1994), as its name suggests, the seed photons come to the jet from external sources such as the accretion disk, the broad-line region (BLR), or the dusty torus.

The object of interest, 3C 454.3, $z = 0.859$, is a blazar and has been classified as an FSRQ due to its high optical variability (Angione 1968) and prominent broad emission lines. This source shows structural and flux variability in its parsec-scale jet (e.g., Pauliny-Toth et al. 1987; Kembell et al. 1996;

Jorstad et al. 2013, 2017) and correlated variability between different wave bands (e.g., Tornikoski et al. 1994; Zhang et al. 2018, 2020). The very high variability of this blazar is a reason for its constant study and for observational campaigns in which 3C 454.3 has been monitored throughout all these years.

The location of the gamma-ray emission region in this object has not been completely determined. Several studies have discussed that the location might be close to the black hole inside the BLR (Poutanen & Stern 2010; Tavecchio et al. 2010; Hu et al. 2015), and others that this emission region should be located outside the BLR downstream of the jet (Sikora et al. 2008; Jorstad et al. 2010; Vittorini et al. 2014; Britto et al. 2016; Coogan et al. 2016). Another important issue that has not reached a consensus is the dominant gamma-ray emission mechanism of 3C 454.3. There are times when it is determined to be EC (Vittorini et al. 2014; Hu et al. 2015), but other studies show indications that SSC is likely to be the dominant mechanism (Kushwaha et al. 2016; Rajput et al. 2019). These studies show that 3C 454.3 could be an example of a source with multiple gamma-ray emission regions, as well as the dominant gamma-ray emission mechanism being able to change.

The link between optical continuum, emission-line variability, and jet kinematics on sub-parsec scales was proposed to be explained by the existence of a jet-excited BLR outflowing downstream of the jet (Arshakian et al. 2010; León-Tavares et al. 2010). León-Tavares et al. (2013) presented direct observational evidence of the BLR close to the radio core of the jet, and this was confirmed in subsequent studies

(Isler et al. 2013; Jorstad et al. 2013). Arshakian et al. (2012) and León-Tavares et al. (2015) present schematics in which this additional BLR (BLR material surrounding the jet) is depicted in contrast to the canonical BLR (virialized clouds located in the inner parsec region of the central engine, e.g., Kaspi et al. 2005). The origin of this additional BLR is still under debate. The most likely origin of this cloud is wind from the accretion disk accelerated by the magnetic field of the jet (Perez et al. 1989). This possibility was individually investigated for 3C 273 (Paltani & Türler 2003) and for 3C 454.3 (Finke & Dermer 2010). Another possible origin is the interaction between the jet and a red giant star stripping its outer shell to enrich the zone (Bosch-Ramon et al. 2012; Khangulyan et al. 2013). The same result can be obtained with a passing star-forming region interacting with the jet (Zacharias et al. 2019).

The highest levels of the Mg II $\lambda 2798$ emission line and the UV Fe II band fluxes and the 2010 gamma-ray outburst happen at the time when a jet component passes through or is ejected from the radio core of 3C 454.3. Similar behavior was observed for CTA 102 but on a greater scale (Chavushyan et al. 2020). The ratio between the maximum of the $\lambda 3000$ continuum flux and its minimum was ~ 179 , and ratios between maximum and minimum for the Mg II emission line and the UV Fe II fluxes were ~ 8 and ~ 34 , respectively.

In this study, we analyze the variability of the gamma-rays, X-rays, V-band, J-band, 1 mm, and 15 GHz light curves, in addition to the flux of the broad emission lines, specifically the Mg II $\lambda 2798$ emission line and the UV Fe II band from the optical spectra, as well as the $\lambda 3000$ continuum. The main goal of this work is to investigate the behaviors of these features to understand the physical conditions and processes that occurred during the periods of high activity of 3C 454.3.

The cosmological parameters adopted throughout this paper are $H_0 = 71 \text{ km s}^{-1} \text{ Mpc}^{-1}$, $\Omega_\Lambda = 0.73$, $\Omega_m = 0.27$. At the redshift of the source, $z = 0.859$, the spatial scale of $1''$ corresponds to a physical scale of 7.7 kpc and the luminosity distance is 5.489 Gpc.

2. Observations

The ground-based observational support of the Fermi Gamma-Ray Space Telescope at the University of Arizona has been monitoring 3C 454.3 over the years as part of its program. Taking advantage of this great collection of data, in this work we used 529 optical spectra observed from 2009–2018 calibrated against the V-band magnitude; see Smith et al. (2009) for further details of the observational setup and the data reduction process. The spectra were taken to the rest frame of the object and a cosmological correction of the form $(1+z)^3$ was applied to the flux (e.g., Peterson 1997). Galactic reddening correction was not applied since we are only interested in the relative flux changes. An important task in this work was to measure the flux of Mg II $\lambda 2798$; to achieve this we had to subtract the UV Fe II emission band and the continuum. The process of spectral fitting was done using the SPECFIT task from the IRAF package.

First, the continuum was approximated as a power-law function to subtract it from the spectrum. Next, the Fe II emission was also subtracted by fitting it using the template of Vestergaard & Wilkes (2001). After performing this process for all the spectra, we integrated the Mg II line profile in the range 2725–2875 Å to obtain its flux. We measured the Fe II flux by integrating the spectrum free of the continuum and the Mg II

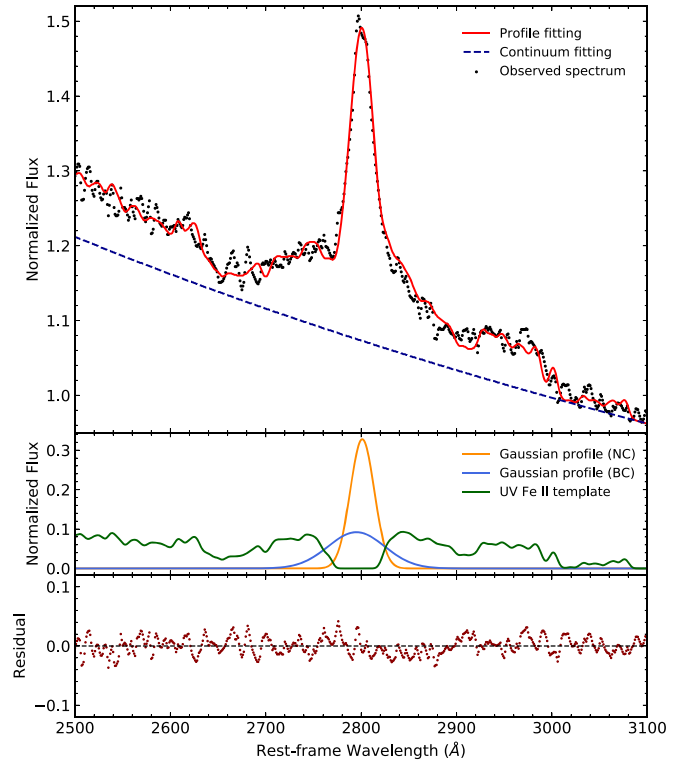


Figure 1. Example decomposition of the Mg II $\lambda 2798$ emission line and the UV Fe II band in the spectrum of a low continuum state taken at the Steward Observatory on 2013 May 10. Top panel: observed spectrum with the obtained best fit; the continuum is shown as a power-law function. Middle panel: the broad and narrow components used to fit the Mg II $\lambda 2798$ line, as well as the UV Fe II template. Bottom panel: the residuals from the subtraction of the best fit from the observed spectrum.

contribution in the range 2850–3000 Å. A third feature obtained from the spectra was the flux of the UV continuum at 3000 Å, which consisted of taking the average value in the range 2950–3050 Å from the iron-subtracted spectrum. An example of the spectral decomposition is illustrated in Figure 1. Unfortunately, we were not able to perform an analysis of the evolution of the Mg II emission line FWHM, since the spectra were taken with different slit sizes ($3''$ being the smallest and $7''.6$ the largest).

There are two unique contributions to the corresponding uncertainty in the Mg II flux measurement. The first and main contribution is the random error, produced in this case by the dispersion and the signal-to-noise ratio of the spectra, which was estimated as in Tresse et al. (1999). The second contribution is introduced by the subtraction of the Fe II emission, estimated as in León-Tavares et al. (2013), considering that no iron subtraction was performed in the range 2786–2805 Å. For the corresponding error in the Fe II flux, the only contribution is the one due to the random error, estimated similarly to that for Mg II. Lastly, the error for the estimation of the $\lambda 3000$ continuum flux was calculated by taking the rms of the iron-subtracted spectrum around $3000 \pm 50 \text{ Å}$. For further details, see León-Tavares et al. (2013) and Chavushyan et al. (2020). A sample of the measured fluxes and errors is displayed in Table 1. The complete table is available in the online journal in machine-readable format.

The gamma-ray light curve was built using the data from the public database of the Fermi Large Area Telescope (LAT,

Table 1Sample of the Flux Measurements for the $\lambda 3000$ Continuum, the Mg II $\lambda 2798$ Emission Line, and the UV Fe II Band

JD – 2,450,000	Flux Continuum $\lambda 3000$ (10^{-13} erg s $^{-1}$ cm $^{-2}$ Å $^{-1}$)	Flux Mg II $\lambda 2798$ (10^{-13} erg s $^{-1}$ cm $^{-2}$)	Flux UV Fe II (10^{-13} erg s $^{-1}$ cm $^{-2}$)
5086.84	0.200 \pm 0.004	1.26 \pm 0.14	0.56 \pm 0.17
5088.76	0.235 \pm 0.004	1.28 \pm 0.14	0.85 \pm 0.17
5088.90	0.215 \pm 0.004	1.22 \pm 0.13	0.76 \pm 0.16
5089.68	0.186 \pm 0.004	1.23 \pm 0.13	0.66 \pm 0.16
5089.81	0.184 \pm 0.003	1.23 \pm 0.11	0.64 \pm 0.13
5089.94	0.184 \pm 0.004	1.19 \pm 0.15	0.66 \pm 0.19
5090.68	0.194 \pm 0.003	1.26 \pm 0.09	0.66 \pm 0.11
5090.81	0.197 \pm 0.004	1.17 \pm 0.14	0.54 \pm 0.17
5090.94	0.204 \pm 0.004	1.22 \pm 0.14	0.71 \pm 0.18
5091.66	0.267 \pm 0.005	1.13 \pm 0.17	0.73 \pm 0.20

(This table is available in its entirety in machine-readable form.)

Abdo et al. 2009) in the energy range 0.1–300 GeV with *Fermitools* version 1.0.2. All sources within 15° of the location of 3C 454.3 were included in the model, taken from the 4FGL catalog (The Fermi-LAT collaboration 2020). The X-ray data were obtained from the public database of the Swift X-Ray Telescope (XRT). The Swift-XRT data were processed using the standard SWIFT tools (Swift Software version 3.9, *FTOOLS* version 6.12 and *XSPEC* version 12.7.1) and the light curves were generated with *xrtgrblc* version 1.6. Details of the reduction procedure can be found in Stroh & Falcone (2013). We took the optical V-band data from two sources: the ground-based observational support of the Fermi Gamma-Ray Space Telescope at the University of Arizona (Steward Observatory, Smith et al. 2009) and the Small and Moderate Aperture Research Telescope System (SMARTS, Bonning et al. 2012). The near-infrared (NIR) J-band data were obtained from SMARTS as well. The 1 mm data were obtained from the Submillimeter Array (SMA) public database. The observations and data reduction details can be found in Gurwell et al. (2007). We used the 15 GHz data from the Owens Valley Radio Observatory (OVRO, Richards et al. 2011) public database. The degree of optical linear polarization and the optical polarization angle were retrieved from the Steward Observatory. The light curves of all the described data are shown in Figure 2.

3. Cross-correlation Analysis

3.1. Cross-correlations for the Complete Data Set

Cross-correlation analysis was performed to determine the time delay between the emissions of the different bands. Only time delays with a correlation coefficient above the 99% significance level were considered. Three different methods were used to ensure the truthfulness of the results, following the methodology in Patiño-Álvarez et al. (2018). Furthermore, a check for aliases via Fourier analysis was conducted to identify and remove these from the results (Press et al. 2007).³ After the alias check, some cross-correlation analyses showed more than one time delay. These were included in the results as well. From visual inspection in Figure 2, we notice that there is a time delay consistent with zero between the gamma-rays, V-

band, J-band, and the $\lambda 3000$ continuum emission, which was confirmed through the cross-correlation analysis. This result indicates that the emission regions of the continuum, the V-band, and the J-band, as well as the source of the seed photons responsible for the IC scattering, are co-spatial. Furthermore, the Mg II $\lambda 2798$ emission line presents anticorrelations against the gamma-rays at 279.9 ± 8.8 days, the $\lambda 3000$ continuum at 19.8 ± 4.2 days (continuum vs. Mg II), and the Fe II at -15.9 ± 4.2 days. The Mg II presents a significant correlation with the $\lambda 3000$ continuum at a time delay of 637.6 ± 4.2 days (continuum vs Mg II), which is consistent with the value (621 ± 45 days) reported by Nalewajko et al. (2019). The UV Fe II band presents correlations at a time delay consistent with zero against the continuum, gamma-rays, and Mg II emission; however, there is a correlation with the continuum at a time delay of 576.9 ± 4.2 days (continuum vs Fe II). Moreover, the Fe II also presents anticorrelations: the one mentioned above with Mg II and with the continuum at a time delay of 20.4 ± 4.2 days (continuum vs Fe II). The full cross-correlation results are shown in Table 2. Some of the resulting figures from the cross-correlations are displayed in Figure 8. The remaining figures are available in the online journal.

3.2. Cross-correlations for the Separate Flaring Periods

Aiming to understand some of the time delays found in the cross-correlations done for the complete data set, and with the purpose of finding the dominant gamma-ray emission mechanism for each flaring period, we selected two sets of observations from the light curves (Figure 2), considering the high activity states in the UV continuum. The period $5000 < \text{JD} - 2,450,000 < 5600$ (flaring period 1, FP1) and the period $6600 < \text{JD} - 2,450,000 < 7900$ (flaring period 2, FP2) are marked in Figure 2 with gray vertical stripes. We performed the cross-correlations between the gamma-rays and V-band, as well as the Mg II, UV Fe II, and $\lambda 3000$ continuum. For FP1, we did not find anticorrelation between any of the light curves. The results show a time delay not consistent with zero for gamma-rays against the UV continuum and the Fe II. For FP2, we found an anticorrelation between the Mg II and the UV continuum at 44.64 ± 4.59 days. This time the gamma-rays correlate with the UV continuum and Fe II at a time delay consistent with zero. We found that the Fe II correlates with the UV continuum at a time delay consistent with zero in both periods. It is important to note that the Mg II does not correlate with the gamma-rays in either of the periods. The cross-correlation results for this analysis are shown in Table 3. Some of the resulting figures from the cross-correlations for FP1 and FP2 are displayed in Figures 9 and 10, respectively. The remaining figures are available in the online journal.

4. Variability

For the two most significant UV-continuum flare-like events, in 2010 (maximum value on $\text{JD} - 2,450,000 = 5510.58$) and 2014 (maximum value on $\text{JD} - 2,450,000 = 6831.96$), the Mg II emission line and the UV Fe II band response were different. On the one hand, during the 2010 event, 3C 454.3 had a major gamma-ray outburst, which had its counterpart in the UV continuum. The Mg II and Fe II both significantly responded to this increase in the ionizing continuum, which corresponds with previous results of León-Tavares et al. (2013), Isler et al. (2013), and more recently Nalewajko et al. (2019). On the other hand,

³ <https://www.cambridge.org/numericalrecipes>

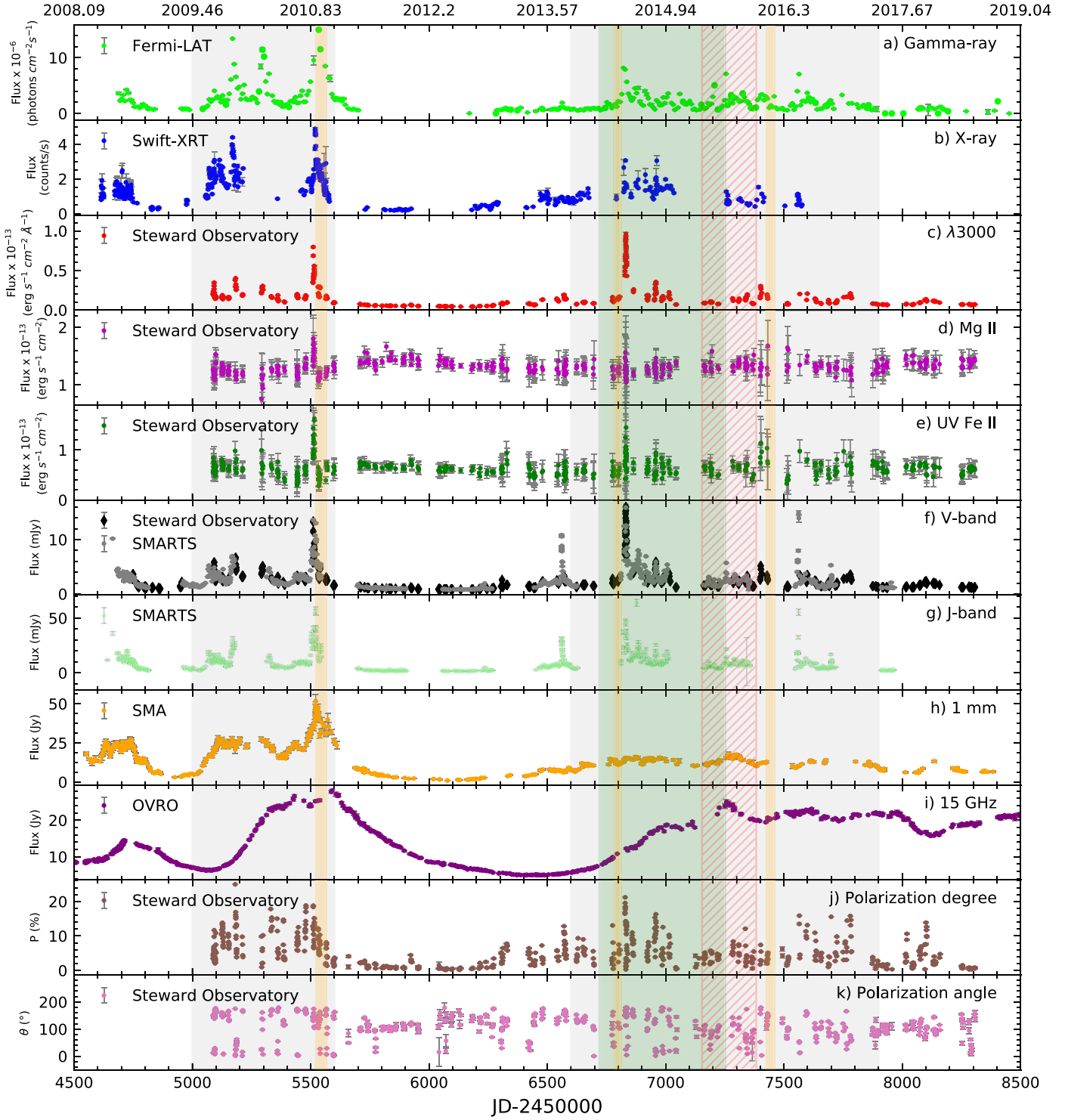


Figure 2. Multiwavelength light curves for 3C 454.3 (see Section 2 for details of the observations). The first and second orange vertical stripes show the time when the knots B11 (Jorstad et al. 2017) and K14 (Lioudakis et al. 2020) were ejected from the radio core, respectively. The third orange vertical stripe represents the time at which the knot K16 (Weaver et al. 2019) crossed the 43 GHz core. The green vertical stripe represents the expected time during which B11 would have passed through the quasi-stationary component (C, Jorstad et al. 2013, 2017). The widths of these stripes represent their respective uncertainty. The red hatched vertical stripe shows the duration of the flare in the 43 GHz flux density of the quasi-stationary component C taken from Figure 7 of Lioudakis et al. (2020). The gray vertical stripes represent the flaring periods as defined in Section 3.2.

during the 2014 event, the source presented a gamma-ray outburst smaller than the one in 2010 but the increase in the UV continuum flux was higher. The Mg II flux did not significantly increase in response to the continuum; a similar behavior was reported by Nalewajko et al. (2019). However, the UV Fe II

presents two flux points in its light curve above 3σ , which suggests that Fe II responded to this flaring event. These results can be seen in Figure 3.

Another tool that can help to understand what was happening during these major events is the nonthermal dominance

Table 2

Cross-correlation Results for the Full Light Curves Given in Time Delays (Days) with Their Uncertainty at 90% Confidence Level

Bands	Delay 1	Delay 2	Delay 3
1 mm vs. 3000 Å	-18.6 ± 16.6
1 mm vs. Fe II	-6.3 ± 4.7
1 mm vs. gamma-rays	-0.1 ± 8.8
1 mm vs. J	-8.2 ± 4.7
1 mm vs. Mg II	Not conclusive
1 mm vs. X-rays	-1.5 ± 5.3
15 GHz vs. 1 mm	-131.6 ± 26.5
15 GHz vs. 3000 Å	Not conclusive
15 GHz vs. Fe II	No correlation
15 GHz vs. gamma-rays	No correlation
15 GHz vs. J	-157.2 ± 2.9
15 GHz vs. Mg II	Not conclusive
15 GHz vs. X-rays	-137.5 ± 5.3
3000 Å vs. Fe II	0.0 ± 4.2	576.9 ± 4.2	20.4 ± 4.2^a
3000 Å vs. gamma-rays	-1.5 ± 8.8
3000 Å vs. Mg II	637.6 ± 4.2	19.8 ± 4.2^a	...
3000 Å vs. X-rays	4.1 ± 5.3	231.5 ± 5.3	...
Mg II vs. gamma-rays	No correlation
Mg II vs. Fe II	2.5 ± 4.2	-15.9 ± 4.2^a	...
Mg II vs. X-rays	-24.4 ± 28.3^a
Fe II vs. gamma-rays	-0.5 ± 8.8
Fe II vs. X-rays	7.2 ± 5.3
J vs. 3000 Å	1.5 ± 4.2
J vs. Fe II	2.25 ± 4.2
J vs. gamma-rays	-0.57 ± 8.8
J vs. Mg II	24.2 ± 4.2^a
J vs. X-rays	1.3 ± 5.3
V vs. 1 mm	10.4 ± 4.7
V vs. 15 GHz	$150.0^{+48.39}_{-39.54}$
V vs. 3000 Å	1.6 ± 4.2
V vs. Fe II	1.6 ± 4.2
V vs. gamma-rays	2.1 ± 8.8
V vs. J	0.1 ± 2.8
V vs. Mg II	21.3 ± 4.2^a
V vs. X-rays	3.9 ± 5.8
V vs. gamma-rays	2.1 ± 8.8
X-rays vs. gamma-rays	4.5 ± 8.8

Notes. All delays have correlations at the $\geq 99\%$ significance level. Delay 2 and Delay 3 are additional delays found to be statistically significant, and are only shown for the cross-correlation analyses in which the delays are not aliases. All cross-correlations are performed in the order stated in this table.

^a Anticorrelation at this delay.

parameter (NTD, Shaw et al. 2012; Patiño-Álvarez et al. 2016; Chavushyan et al. 2020). The calculation of NTD, as its name suggests, constitutes a method to find out if there is a nonthermal contribution (the jet as the source) to the continuum emission. If $NTD = 1$, the continuum emission is purely thermal emission, its specific source being the accretion disk. If NTD lies between 1 and 2 then the dominant source of the continuum is the accretion disk, but some contribution from the jet is expected. The nonthermal emission dominates for values of $NTD > 2$, and if $NTD = 2$ the contributions from the disk and the jet are equal. For the calculation of this parameter, one needs to know the observed continuum luminosity (L_{obs}) and to estimate from the emission line luminosity a predicted continuum luminosity (L_{pred} , expected luminosity of the accretion disk), then $NTD = L_{\text{obs}}/L_{\text{pred}}$. We calculated this predicted continuum luminosity from the bisector fit of the relation between the luminosity of Mg II and the $\lambda 3000$

continuum luminosity found by Shen et al. (2011). In Figure 3(d), we can see that during the high-energy events the NTD value surpasses $NTD = 2$, and during the 2010 and 2014 flares it reaches maximum values of 12.0 and 24.7, respectively. This result indicates that the continuum emission during these flares is vastly dominated by the jet. In Figure 5(c), we can see that NTD increases when the continuum emission luminosity increases, which is expected. Furthermore, just after the 2010 flare ($5700 < JD - 2,450,000 < 6300$) the NTD value oscillates around 1 (the disk is the dominant source of the continuum), which coincides with the gamma-rays (emitted by the jet) not being detected.

The linear optical polarization is a tool for probing the magnetic field in the jet (e.g., Zhang 2019, and references therein). From the observations presented in Figures 2(i) and (j), we can determine that the optical linear degree of polarization reaches its highest values at the time of the major gamma-ray outbursts, indicating that either a shock is compressing an initially turbulent magnetic field (Laing 1980) or a strongly polarized emission zone emerged at the time (Itoh et al. 2013). Equally notable are the large changes in the polarization angle during the periods of high activity; this tells us that the magnetic field of the jet is changing its morphology and even the structure of the jet itself (Marscher et al. 2008; Chandra et al. 2015; Blinov et al. 2018).

At the end of 2010, a blob (B11, Jorstad et al. 2017) was ejected from the 43 GHz core of 3C 454.3 ($JD - 2,450,000 = 5544.25 \pm 21.90$), causing the brightest gamma-ray flare of that year (maximum value on $JD - 2,450,000 = 5512.66$). This ejection is represented by an orange stripe in Figure 2. The deprojected distance from the black hole to the 43 GHz core, estimated with an angle of $1^\circ 3$ (between the jet and our line of sight), is ~ 9 pc (Kutkin et al. 2014). Meanwhile, Jorstad et al. (2010) estimated an upper limit of ~ 18 pc. In this work we will adopt ~ 9 pc as the deprojected distance from the black hole to the 43 GHz core. Using the mean proper motion (0.152 ± 0.012 mas yr^{-1}) of the blob B11 given by Jorstad et al. (2017), which was calculated with 43 GHz observations from very long baseline interferometry, we estimated the time at which it would reach the quasi-stationary component C (at ~ 0.6 mas from the radio core, which corresponds to a projected ~ 4.6 pc, Jorstad et al. 2013, 2017). The expected time at which the blob B11 would have reached the quasi-stationary component C should be $6719.46 \leq JD - 2,450,000 \leq 7252.65$ (green vertical stripe in Figure 2). These quasi-stationary features are typically interpreted as recollimation shocks in an overpressured jet and cannot be explained by traveling shock waves within a pressure-matched and therefore conical jet (Daly & Marscher 1988).

Recently, the ejection was reported of the relativistic component K14 from the 43 GHz core ($JD - 2,450,000 = 6797 \pm 15$), which coincides with the maximum of the gamma-ray flare of 2014 (maximum value on $JD - 2,450,000 = 6821.66$) within 2σ of uncertainty (Liodakis et al. 2020). This ejection is illustrated in Figure 2 with an orange stripe. Additionally, in the bottom panel of Figure 7 of their work, the quasi-stationary component C increased its 43 GHz flux density ~ 9 times during FP2 (maximum value on $JD - 2,450,000 \sim 7287$), which we represent with a red hatched vertical stripe in Figure 2 (the width represents the time from the beginning of the flare until the end of the data in Figure 7 of the authors). We observe this flaring activity in gamma-rays, V -band, and J -band (maximum values on $JD - 2,450,000 = 7255.66$, 7256.68, and 7256.68, respectively) as well. We can see in

Table 3

Cross-correlation Results for the Separate Flaring Periods, as Described in Section 3.2, Given in Time Delays (days) with Their Uncertainty at 90% Confidence Level

	FP1		FP2
Bands	Delay 1	Delay 2	Delay
Mg II vs. 3000 Å	3.8 ± 2.4	...	44.6 ± 4.6^a
Fe II vs. 3000 Å	0.0 ± 2.4	...	0.1 ± 4.6
Fe II vs. Mg II	-2.7 ± 2.4	-36.8 ± 2.4	No correlation
Gamma-rays vs. 3000 Å	-6.6 ± 2.4	...	3.0 ± 4.6
Gamma-rays vs. Fe II	-6.4 ± 2.4	-36.4 ± 2.4	2.6 ± 4.6
Gamma-rays vs. Mg II	No correlation	...	No correlation
V vs. 3000 Å	0.4 ± 2.4	...	0.4 ± 4.6
V vs. Mg II	-1.2 ± 2.4	...	No correlation
V vs. Fe II	-0.2 ± 2.4	...	0.7 ± 4.6
V vs. gamma-rays	3.9 ± 1.5	...	0.6 ± 2.0

Note. All delays have correlations at the $\geq 99\%$ significance level. Delay 2 is an additional delay found to be statistically significant and only shown for the cross-correlation analyses in which the delay is not an alias. All cross-correlations are performed in the order stated in this table.

^a Anticorrelation at this delay.

Figure 2 that the green vertical stripe coincides within its uncertainty with the red hatched vertical stripe. Hence, the estimated collision between the blob B11 and the quasi-stationary component C could explain the origin of the multiwavelength flaring event in the latter.

Weaver et al. (2019) reported an ejection of a relativistic component K16 from the 43 GHz core ~ 4 months before the flaring event of 2016 June (JD $- 2,450,000 = 7448 \pm 17.5$); this component traveled across the radio core and later disappeared. They inferred that electrons were accelerated from a back interaction with the core, causing the variability. This ejection is marked with an orange stripe in Figure 2.

There are noticeable increases in the fluxes of 1 mm and 15 GHz during the periods of high activity of the object in Figure 2. These increases indicate that the main source responsible for the flaring events is the jet (nonthermal emission). The 15 GHz increased its flux by a comparable amount during the two flaring periods. On the other hand, we see that the 1 mm flux increases less in FP2 than during FP1. A similar behavior can be seen for the 22 GHz and 37 GHz light curves in Figure 1 from Sarkar et al. (2019). In an attempt to explain this effect, we estimated the spectral index (α , $S_\nu \propto \nu^\alpha$) with the 15 GHz and 1 mm (adopting 230 GHz as the frequency) flux densities during the quasi-simultaneous epochs and interpolated the 15 GHz light curve into the 1 mm epochs. Both estimates are displayed in Figure 4. In panel (c) of this figure, the dashed line at $\alpha = 0$ (Fromm et al. 2011; Park & Trippie 2014) indicates the separation between optically thin ($\alpha < 0$) and optically thick ($\alpha > 0$). During the 2010 flare, the spectral index indicates that the spectrum is in the optically thick regime. However, by the time of the brightest flare of 2014, the spectral index is very close to the threshold, and after JD $- 2,450,000 \approx 6900$ it goes below zero (optically thin), letting us see a larger region. Furthermore, the lower energy electrons (e.g., 15 GHz) are cooled by synchrotron emission less efficiently than higher energy electrons (e.g., 1 mm), which keeps the more energetic electrons confined in a smaller region. The combination of these factors could be the reason why the 1 mm flux had a smaller response during the second flaring period than during the first.

The variability of the spectral index indicates variations of intricate source properties, most likely changes in the optical depth (Trippie et al. 2011). Along the same lines, Park et al. (2019)

proposed that when the radio spectra are optically thick an emerging component is close to the core, and when the spectra become optically thin the component is well separated from the core. This interpretation describes well what happened during FP1 and is compatible with the shock-in-jet model (e.g., Marscher & Gear 1985; Valtaoja et al. 1992; Fromm et al. 2011; Hughes et al. 2011; Weaver et al. 2019). During FP2, the spectral index is not varying as much as during FP1 and the changes are slower. This could indicate that the spectra are different during these periods, and hence the physical conditions and/or mechanism as well. The more complex nature of FP2, as a result of a superposition of multiple events, might justify the strange behavior of the spectral index. Finally, since there is a flaring behavior of the quasi-stationary component C, in addition to the multiple ejections from the radio core during FP2, we can hypothesize that there are multiple gamma-ray emission regions in the jet of 3C 454.3.

5. Luminosity Relations

5.1. Luminosity Relations for the Complete Data Set

With the purpose of directly comparing the response of the Mg II and Fe II to the $\lambda 3000$ continuum, we calculated their luminosities and plotted them as shown in Figure 5. We performed linear fitting for each luminosity relation using orthogonal distance regression from the `SciPy ODR` package.⁴ A fit was considered statistically significant when the respective p -value (p_v , the probability of obtaining a chi-square value equal or higher by chance) is below 0.05. In panel (a), we can see that the luminosity of the Mg II emission line tends to decrease with increasing luminosity of the continuum, except for the highest luminosities. For the entire data set, we found that the linear fit for this relation was not statistically significant. To find the continuum luminosity up to where the luminosity of Mg II is decreased, we looked for the linear fit to the first 11 points (minimum number for a trustworthy correlation, Alexander 1997), then for 12 and so forth in the direction of increasing continuum luminosity. We found that p_v varied through all the analyses. The last significant linear fit (black line in Figure 5(a)) was at $\log(\lambda L_{\lambda 3000}/\text{erg s}^{-1}) = 47.56$, giving a resulting slope of -0.09 ± 0.01 with $p_v = 0.0329$.

⁴ <https://docs.scipy.org/doc/scipy/reference/odr.html>

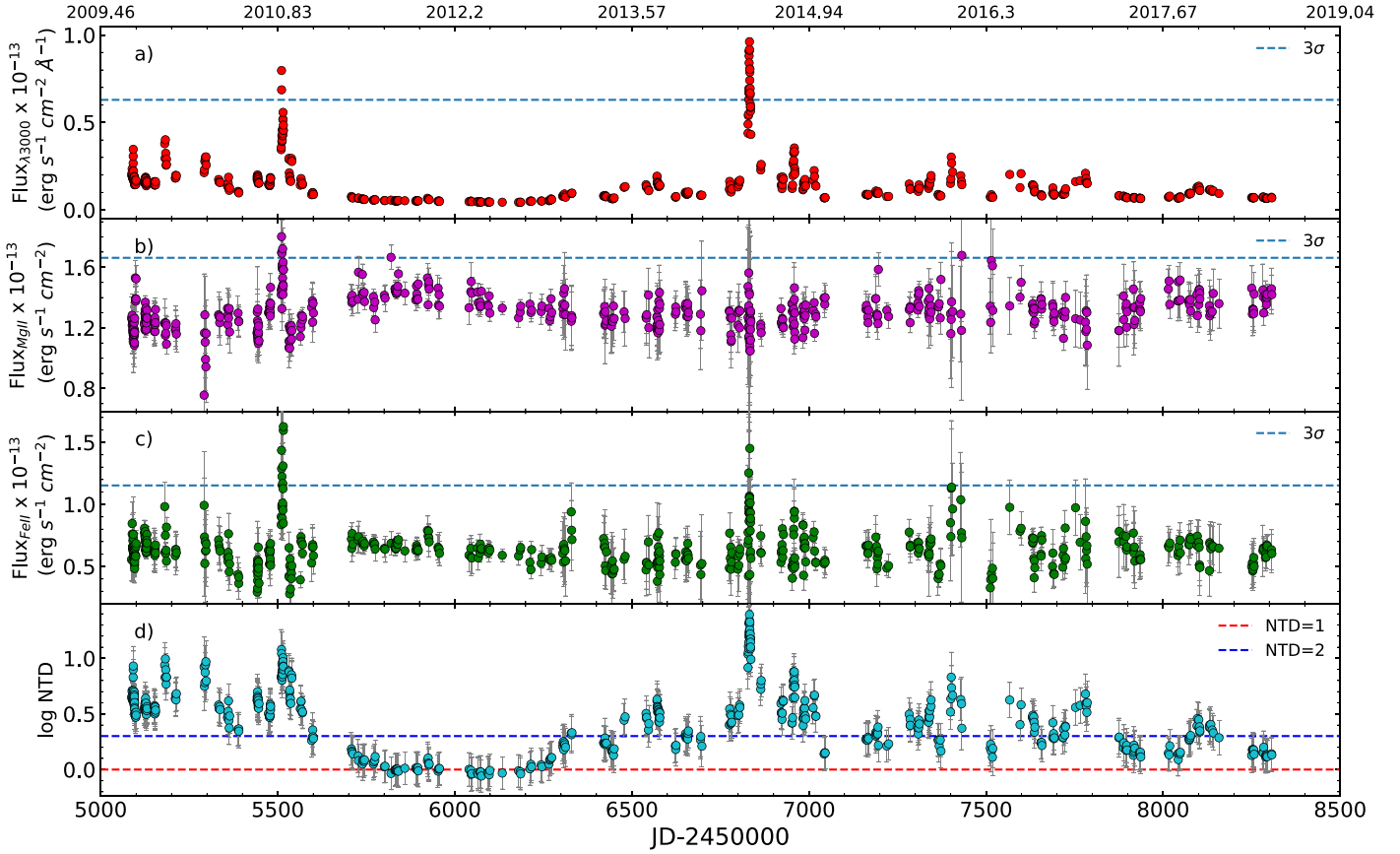


Figure 3. Light curves of (a) the $\lambda 3000$ continuum flux, (b) the Mg II $\lambda 2798$ emission line flux, (c) the UV Fe II band flux, and (d) the NTD parameter on a logarithmic scale. In the first three panels, the blue dashed line represents 3σ . The red and blue dashed lines in (d) represent $\text{NTD} = 1$ and $\text{NTD} = 2$, respectively.

Additionally, we performed a Spearman correlation rank test and found a significant anticorrelation ($\rho = -0.41$, $p_v = 2 \times 10^{-23}$). In the case of the Spearman correlation, p_v refers to the probability of obtaining a correlation coefficient equal or higher by chance.

For Fe II in Figure 5(b), we cannot see a clear behavior at first glance, hence we performed the same analysis as done for Mg II. The last statistically significant linear fit (black line in Figure 5(b)) was at $\log(\lambda L_{\lambda 3000} / \text{erg s}^{-1}) = 47.69$, giving a resulting slope of 0.06 ± 0.01 with $p_v = 0.037$; above this threshold the fit becomes non-significant. The Spearman test shows that there is a weak correlation ($\rho = 0.25$, $p_v = 4 \times 10^{-9}$); it is important to note that ρ^2 is less than the error rate for almost all the points (any correlated variability has a lower amplitude than the uncertainty).

Since the object has two different phases, disk dominance and jet dominance, we explored the same relations between the Mg II and Fe II luminosities against the ionizing continuum to find whether the disk or the jet is responsible for the above correlations. We separated the data into two sets, one containing the points when $\text{NTD} < 2$ and the other when $\text{NTD} > 2$. The $\text{NTD} < 2$ data set contains 187 points, corresponding to 35% of the total observation points, which means that in 65% of the observing time the jet is the dominant source of the continuum. During the phase of disk dominance, the Spearman test shows that there is no correlation between the continuum and the spectral features, except for a weak anticorrelation between the continuum and the Mg II ($\rho = -0.20$, $p_v = 0.004$). However, during the phase of jet dominance, we found that there is a significant correlation between the continuum and the Fe II luminosities

($\rho = 0.39$, $p_v = 7 \times 10^{-14}$), and likewise with the ratio between Fe II and Mg II luminosities ($\rho = 0.47$, $p_v = 6 \times 10^{-20}$). Again, between the continuum and Mg II, there is a weak anticorrelation ($\rho = -0.15$, $p_v = 0.005$).

5.2. Luminosity Relations for the Separate Periods of Flares

The analysis done in the last subsection showed that we cannot determine a behavior that describes all the observations. This led us to analyze the luminosity relations separated by the flaring periods. We selected the luminosity observations during the same periods described in Section 3.2. These now separated luminosity relations are displayed in Figure 6. The left panel corresponds to the luminosities during FP1 and the right panel to FP2. The luminosities of the Mg II emission line and the UV Fe II band do not vary monotonically with increasing continuum luminosity during FP1. However, during FP2 there is a clear trend. The linear fit for each luminosity relation during FP2 was no trouble to find; additionally, we calculated their Spearman correlation coefficient. The linear fit of the relation for the Mg II, displayed in Figure 6(a2), gives a slope of -0.05 ± 0.01 with $p_v = 2 \times 10^{-5}$ and we found a weak anticorrelation ($\rho = -0.27$, $p_v = 0.0002$). For the Fe II, in panel (b2), the slope is 0.15 ± 0.03 with $p_v = 0.024$ and we found a significant correlation ($\rho = 0.52$, $p_v = 2 \times 10^{-14}$). Finally, for the ratio Fe II/Mg II, in panel (c2), the slope found is 0.18 ± 0.030 with $p_v = 1 \times 10^{-5}$ and the correlation found was significant ($\rho = 0.56$, $p_v = 4 \times 10^{-17}$) as well.

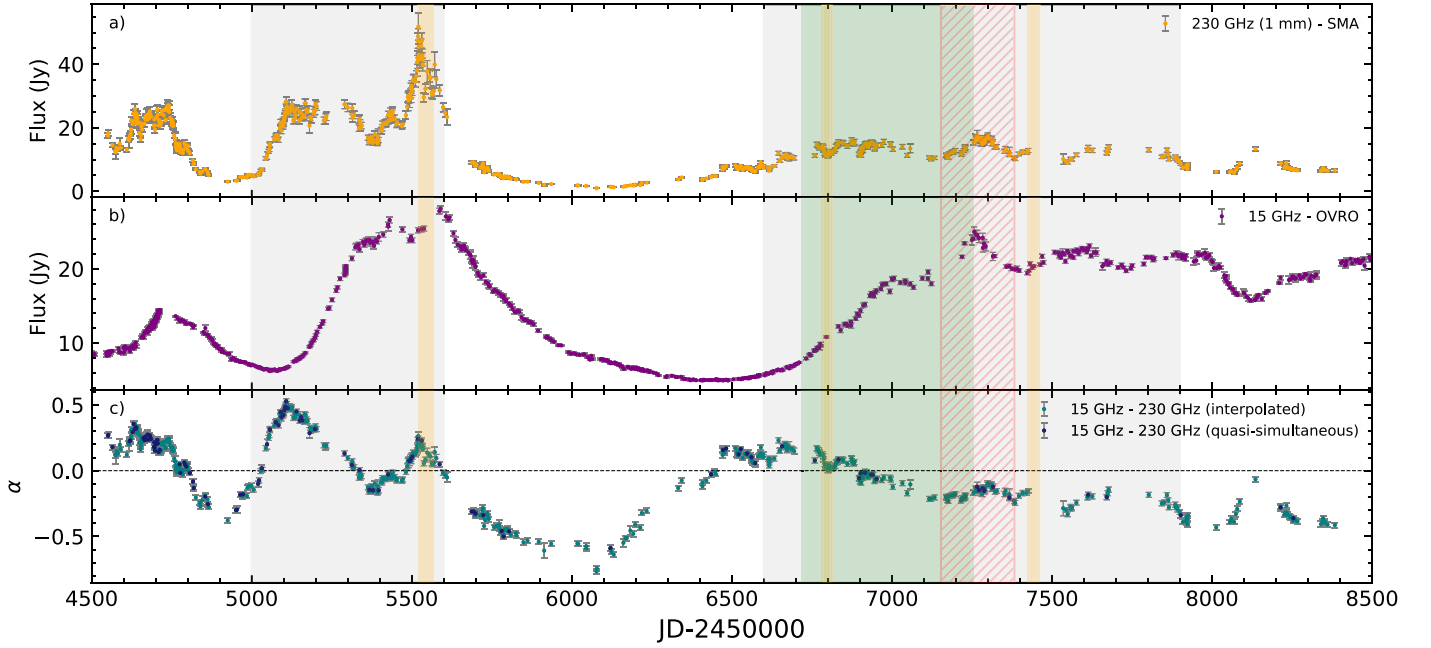


Figure 4. Light curves of (a) 1 mm from the public database of the SMA and (b) 15 GHz from the OVRO. (c) The spectral index (α , $S_\nu \propto \nu^\alpha$) estimated with the 15 GHz and 1 mm (we adopted 230 GHz) flux densities. The teal points correspond to the spectral indices estimated through interpolation and the dark blue points correspond to the spectral indices estimated only at quasi-simultaneous epochs. The horizontal dashed line is at $\alpha = 0$. The vertical stripes represent the same as in Figure 2.

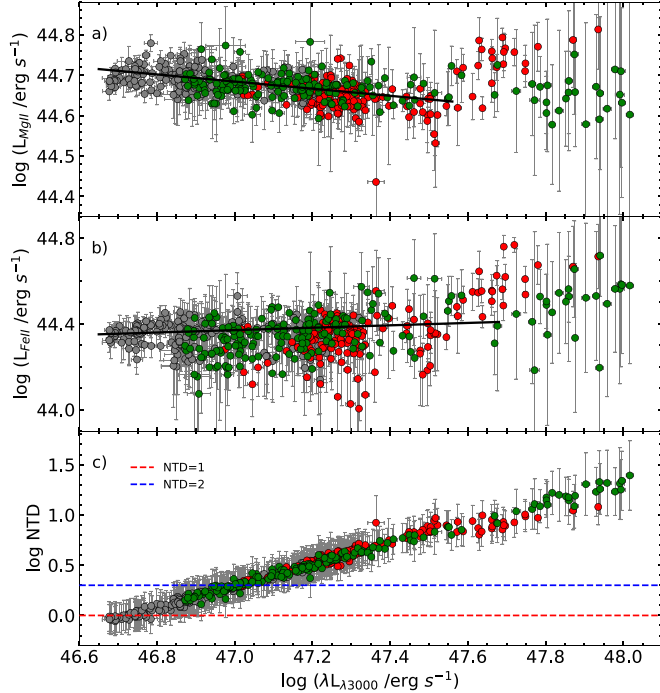


Figure 5. Variations of $\lambda 3000$ continuum luminosity compared to (a) the Mg II $\lambda 2798$ emission-line luminosity, (b) the UV Fe II band luminosity, and (c) the NTD parameter on a logarithmic scale; NTD = 1 and NTD = 2 are represented by red and blue dashed lines, respectively. The last statistically significant linear fit (see Section 5.1) is represented by the black line in panels (a) and (b). The colors indicate the period of observation: green corresponds to the observations during FP1 (see Section 3.2), red to observations during FP2 (see Section 3.2), and gray to the remaining observing points.

From Figure 5, we can see that at low continuum luminosities until some value (threshold), the observations from FP1 are indistinguishable from those for FP2, then they

start to act differently at high continuum luminosities. For the luminosity relations of FP1, in the left panel of Figure 6, we found the linear fit below and above a determined continuum luminosity threshold in the following way: if the data set has N points, we calculated the linear fit for the first 11 points (see Section 5.1) and the next $N - 11$, then again but for the first 12 and the next $N - 12$ and so forth, ending with multiple linear fits for below and above the different thresholds. Finally, we found that until $\log(\lambda L_{\lambda 3000} / \text{erg s}^{-1}) = 47.44$, for both the Mg II and Fe II, the slope is consistent with the one found for the respective data sets of FP2. The black dashed lines on top of the FP1 relations in the left panel of Figure 6 correspond to the best fits for the FP2 relations (black solid lines in the right panel). For the Mg II, displayed in Figure 6(a1), we found below the threshold a slope of -0.04 ± 0.04 with $p_v = 0.182$ (linear fit not accurate), and above the threshold a slope of 0.58 ± 0.07 with $p_v = 0.724$ (linear fit not accurate). The Spearman correlation test shows a significant anticorrelation ($\rho = -0.32$, $p_v = 0.0003$) below the threshold and a strong and significant correlation ($\rho = 0.79$, $p_v = 5 \times 10^{-9}$) above. For the Fe II, in Figure 6(b1), below the threshold the slope found was 0.17 ± 0.09 with a $p_v = 0.107$ (linear fit not accurate), and above the threshold, we found a slope of 1.18 ± 0.16 with $p_v = 0.999$ (linear fit not accurate). The Spearman correlation test indicates that below the threshold there is a weak correlation ($\rho = 0.18$, $p_v = 0.046$) and above it there is a very strong and significant correlation ($\rho = 0.84$, $p_v = 4 \times 10^{-11}$). The lines depicted for the ratio Fe II/Mg II, in Figure 6(c1), are simply the quotient of the linear fits found for the Mg II and Fe II individually, and the Spearman correlation test shows that below the threshold there is a weak but significant correlation ($\rho = 0.28$, $p_v = 0.002$) and above it there is a strong and significant correlation ($\rho = 0.63$, $p_v = 3 \times 10^{-5}$). We sought a luminosity threshold for FP2, but the analysis did not show a clear difference between the behaviors at low and high continuum luminosities.

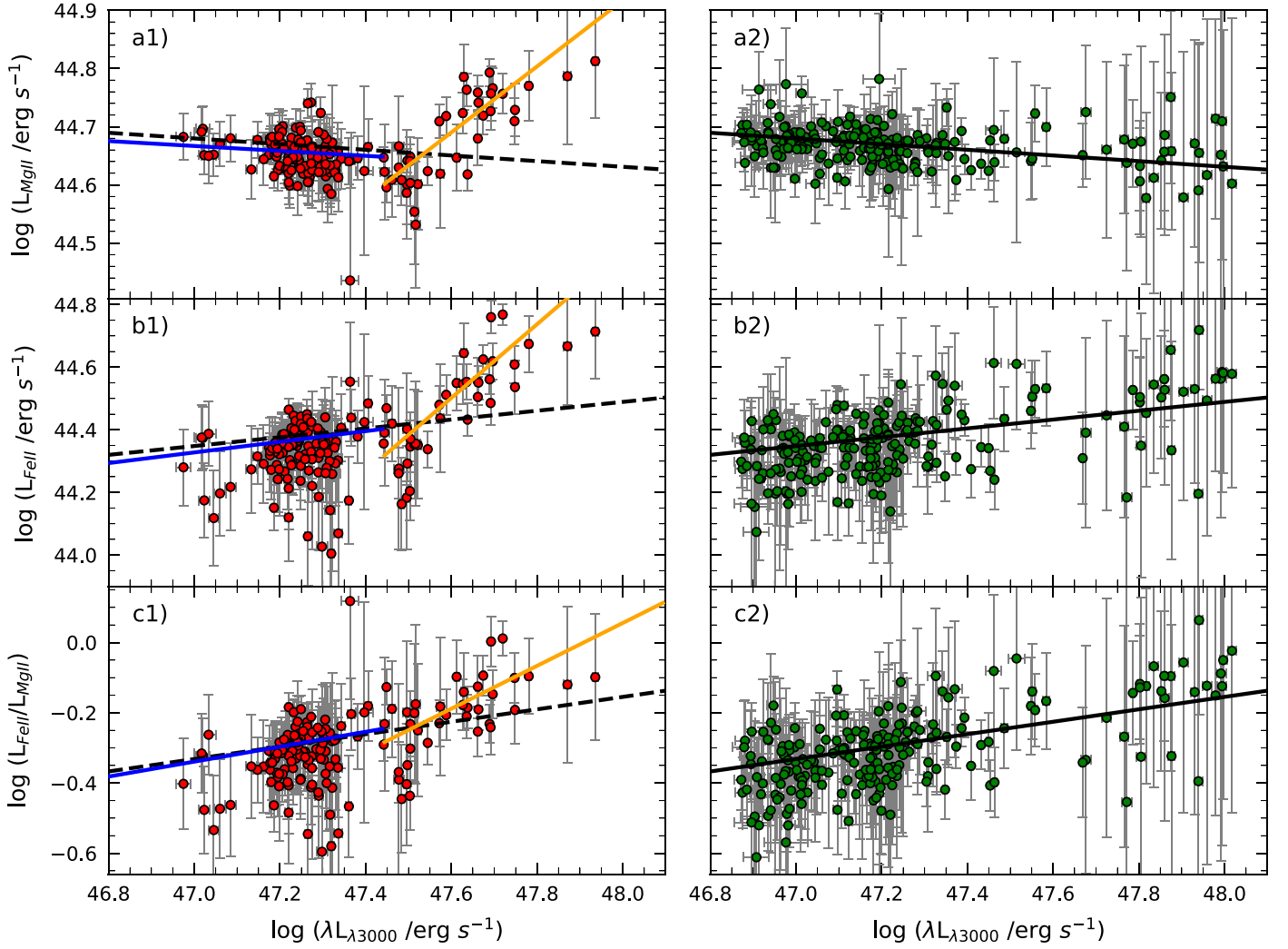


Figure 6. Left panel: luminosity relations corresponding to FP1 described in Section 5.2. Right panel: luminosity relations corresponding to FP2. (a1) and (a2): variations of the Mg II $\lambda 2798$ emission line depending on the $\lambda 3000$ continuum luminosity. (b1) and (b2): variations of the UV Fe II band depending on the $\lambda 3000$ continuum luminosity. (c1) and (c2): the ratio between the UV Fe II and the Mg II $\lambda 2798$ luminosities varying with the $\lambda 3000$ continuum luminosity. The linear fit, in (a1) and (b1), from the beginning to the threshold ($\log(\lambda L_{\lambda 3000} / \text{erg s}^{-1}) = 47.44$) is represented by the blue line while the linear fit from the same threshold to the final point is represented by the orange line. In (c1), the blue and orange lines represent the quotient of the respective linear fits in (a1) and (b1). The full linear fit for each luminosity relation of FP2 is represented by a black solid line in the right panel, and by a black dashed line in the left panel.

6. Discussion

6.1. Location of the Emission Region and Dominant Emission Mechanism of the Gamma-Rays

The brightest flares of 2010 and 2014 were both produced by the ejection of a blob (B11 and K14, respectively) from the 43 GHz core. However, the quasi-stationary component C presented a flaring event after the 2014 flare. As showed in Section 4, FP2 was a superposition of multiple events at different locations. Supporting this, the spectral index varied more rapidly during FP1 than during FP2 since the latter seems to be more complex, hence the physical conditions and/or processes that produced the spectra were different at these periods. This suggests that there are multiple gamma-ray emission regions in 3C 454.3. A change of the location of the gamma-ray emission region of the FSRQ 3C 279 was suggested by Patiño-Álvarez et al. (2018) and later observed (Patiño-Álvarez et al. 2019); they confirmed the location of a non-stationary gamma-ray emission zone at a distance of at least 42 pc from the core. Furthermore, they suggest that the

dominant gamma-ray emission mechanism from this zone is most probably SSC.

Another important aspect to discuss is the dominant gamma-ray emission mechanism during the different periods. Shah et al. (2017) found that to explain the gamma-ray emission of 3C 454.3, both emission mechanisms need to be considered—EC and SSC. This has been proposed for FSRQs in general as well (Zacharias & Schlickeiser 2012; Zhang & Fan 2018). However, for the FSRQ PKS 1510-089, Chen et al. (2012) could not firmly discriminate between the two mechanisms for the gamma-ray emission. From our cross-correlation analysis, we found for FP1 time delays of a few days between the gamma-rays, the UV continuum, and the Fe II. Janiak et al. (2012) found that delays of a few days (for 3C 279) are well explained when EC is the dominant gamma-ray emission mechanism. If we interpret our delays in the same manner, it would mean that the dominant contribution of seed photons for FP1 is coming from external sources (the additional BLR, e.g., León-Tavares et al. 2013). This is consistent with the results found in the literature (Vitorini et al. 2014; Hu et al. 2015).

Recently, Das et al. (2020), using a single-zone model and assuming that the gamma-ray emission region is in the BLR, determined that the dominant mechanism for FP1 is EC. However, the gamma-ray emission region for this event should be at ~ 9 pc from the black hole (location of the 43 GHz core). Multizone models have been proposed to address this issue. One example is when the beamed synchrotron radiation, after scattering off a cloud near the jet trajectory and re-entering the jet, can be an important source of photons causing a flaring event (Ghisellini & Madau 1996; Böttcher & Dermer 1998). This mirror-like model has been applied to explain the brightest gamma-ray flare of 2010 (Vitorini et al. 2014; Tavani et al. 2015) with the additional BLR as the mirror and the dominant gamma-ray emission mechanism as EC.

Our cross-correlation results for FP2 are consistent with no time delay between the same wavelengths. Thinking along the same lines as for FP1, zero time delay would indicate that the region emitting seed photons is co-spatial with that emitting gamma-rays.

For FP2 we do not see the same significant response from the Mg II (but we do for the Fe II) as during FP1 and there might be multiple gamma-ray emission regions. Ghisellini et al. (2005) applied the spine-sheath model to fit the SEDs of TeV BL Lac objects. This is a multizone alternative to the homogeneous SSC allowing less extreme physical parameters. Each component would see an enhanced radiation field coming from the other component (these components are co-spatial), boosting the IC radiation (with respect to a homogeneous jet). At large distances, the conditions of the jets of FSRQs and BL Lacs could be comparable. This model has been invoked to explain the origin of gamma-ray flares in PKS 1510-089 (e.g., Marscher et al. 2010; Park et al. 2019). Particularly, the gamma-ray flare of 2015 from this object was found to originate at ~ 10 pc from the base of the jet. Park et al. (2019) attempted to explain this with the spine-sheath model; however, they suggest that for this particular case the jet might consist of multiple layers (not just a fast spine and a slow sheath). A toy model of a spine-sheath structured jet has been developed for FSRQs by Sikora et al. (2016). They demonstrate that it provides a natural explanation for the hardness and the extreme Compton dominance of the gamma-ray flares, and the weaker fractional flux variations in the optical band than those in gamma-rays. The model allows one to follow the dependence of different radiation spectral components on the physical parameters.

Our results indicate that the physical conditions during these two flaring periods were different. The locations and the gamma-ray emission mechanism would have changed for the different flares in the two flaring periods. A similar behavior was found by Patiño-Álvarez et al. (2018) for 3C 279. Finally, to confirm the nature of each significant flare during FP2, a study of the SED shape using a multizone jet emission model (e.g., multizone turbulent jet, Marscher 2014; Peirson & Romani 2018, 2019) with realistic and well defined parameters needs to be performed.

6.2. The Difference in the Behavior of Mg II and Fe II

From the cross-correlation analysis, we found a delay of ~ 640 days between the $\lambda 3000$ continuum and the Mg II $\lambda 2798$ emission line and a delay of ~ 580 days for the continuum against the UV Fe II. Nalewajko et al. (2019) found a similar

delay for the Mg II and used it to calculate the BLR size ($\Delta r \sim 0.28$ pc), interpreting the delay as the reverberation of the accretion disk emission. However, we have determined that for most of the UV-continuum light curve the dominant emitting source is the jet. Furthermore, the BLR material that is being ionized does not correspond solely to the canonical BLR, but to an additional BLR surrounding the jet as well (e.g., León-Tavares et al. 2013). Hence, we believe these delays should not be used for reverberation mapping since we cannot know exactly what is causing them.

The luminosity relations showed that the jet is responsible for the major increase in the continuum, and from the light curves we found that the Mg II $\lambda 2798$ emission line does not increase its flux significantly during the 2014 flare, while the UV Fe II band does. However, neither the jet nor the disk apparently has a major effect in the Mg, and if there is any effect it is an anticorrelation, implying that when the continuum increases, the Mg decreases, although the jet seems to be the source of the continuum that is ionizing the Fe. To explain the anticorrelation of the Mg II with the continuum, Nalewajko et al. (2019) propose that the continuum has a destructive ionization effect in Mg. But, since we do not see this same effect in the Fe II, it is important to understand the differences between Mg and Fe to find an explanation. The abundances of Mg and Fe might be unequal, affecting the fluxes of the Mg II emission line and the UV Fe II band. This possibility was studied by Verner et al. (2003). Another explanation could be the location of Mg and Fe. Since the ionization potentials of the Mg II and the Fe II are very similar (7.6 and 7.9 eV, respectively), it is assumed that the Mg II and the UV Fe II emission originate in a partially ionized zone of the cloud (Dietrich et al. 2003 and references therein). However, Wills et al. (1985) proposed that they are emitted in different zones, the Mg zone being much less extended than that of Fe. This extended zone of Fe should contain hot regions where the Mg is already ionized, emitting Mg II much less efficiently. Baldwin et al. (2004) propose that the UV Fe II emission comes from a different component in which Fe is collisionally ionized. This gas would not emit lines of other elements strongly, hence it would have to be a different BLR component. An additional important difference between Mg and Fe is that they have distinct properties of radiative transfer. The principal difference is the number of resonance lines, Mg II $\lambda 2798$ being a doublet while Fe II involves thousands of transitions. This is due to Fe II being subject to multiple processes (line fluorescence, Ly α pumping, and turbulence, Verner et al. 1999, 2003). As a consequence, Wills et al. (1985) found that Balmer continuum destruction affects the Mg II much more than the Fe II. Therefore, for each optically thick Fe II resonance line there are many escape routes, through conversion to others with smaller optical depths.

6.3. The Difference in the Behavior of the Spectral Features in the Different Periods

The cross-correlations of the full data set showed an anticorrelation at ~ 20 days for the $\lambda 3000$ continuum against the Mg II $\lambda 2798$ emission line and the UV Fe II band. However, when we divided the data set into two periods and performed the cross-correlations for each, these anticorrelations disappeared. A new anticorrelation between the UV continuum and the Mg II at a delay of ~ 45 days appeared, but only for FP2.

We can interpret this again as a destructive ionizing continuum acting upon the Mg.

We found that the response of either of the spectral features changed from FP1 to FP2. For the calculation of the linear fits for each luminosity relation of FP1, we determined that the behavior of the spectral features in FP2 was the same as during FP1 but at low continuum luminosities. This result can be interpreted as follows: during FP2 we see that the Mg II and Fe II have a monotonic behavior, which tells us that the BLR material is not responding strongly to the increasing continuum. However, we see some increase of the Fe II. In FP1 below the threshold we see the same weak response, but above the threshold we see that both the Mg II and the Fe II respond strongly to the increasing continuum. This indicates that the nonthermal continuum is ionizing the additional BLR efficiently. Chavushyan et al. (2020), for CTA 102, found a threshold in the luminosity relations between the Mg II and Fe II against the continuum. However, the threshold in that source indicates the separation from when the Mg II and Fe II are not responding to when they start to present a clear increase in the flux. The authors interpret this behavior as indicating that the material from the canonical BLR is completely ionized below the threshold (the disk being the dominant source of ionizing continuum), but above it the continuum (the jet being the dominant source) is able to ionize the BLR material near the jet. In that case, the ionizing continuum, being destructive upon the Mg II, is not observed (the features do not show anticorrelations).

Three possible scenarios might explain why we see a difference in the response of the Mg II and Fe II from FP1 to FP2.

The first scenario is that there is a difference in the ionizing spectrum produced by the different physical conditions during the flaring periods. During FP1 the gamma-ray emission region is at the radio core. Yet during FP2 we might have multiple gamma-ray emission locations: ejections from the radio core and a collision at the quasi-stationary component C.

The second scenario is a difference in the state of the additional BLR. During FP1, we see a strong response of Mg II and Fe II to the increase in the ionizing continuum, meaning that the BLR material surrounding the jet is present and could be ionized (León-Tavares et al. 2013). But during FP2, the behaviors of the luminosity of the Mg II (decreasing) and the Fe II (increasing) do not display any major changes at high continuum luminosities. In this scenario, the weak responses when the ionizing continuum increases indicate that there is not enough BLR material to be ionized by the jet. The material that was ionized during the FP1 flare could have mostly dissipated due to interaction with the medium by the time of FP2.

The third scenario is related to the location of the additional BLR. These BLR clouds could be at a different location during FP2, making the ionization of the Mg II and Fe II more difficult. This additional BLR could have been an important source of seed photons for the IC to produce gamma-rays during FP1. However, if the BLR clouds by the time of FP2 are located farther from the radio core, the dominant source of the required seed photons for IC to produce the gamma-rays could be the jet itself (e.g., spine-sheath model).

Finally, it needs to be considered that a combination of these scenarios may also be possible.

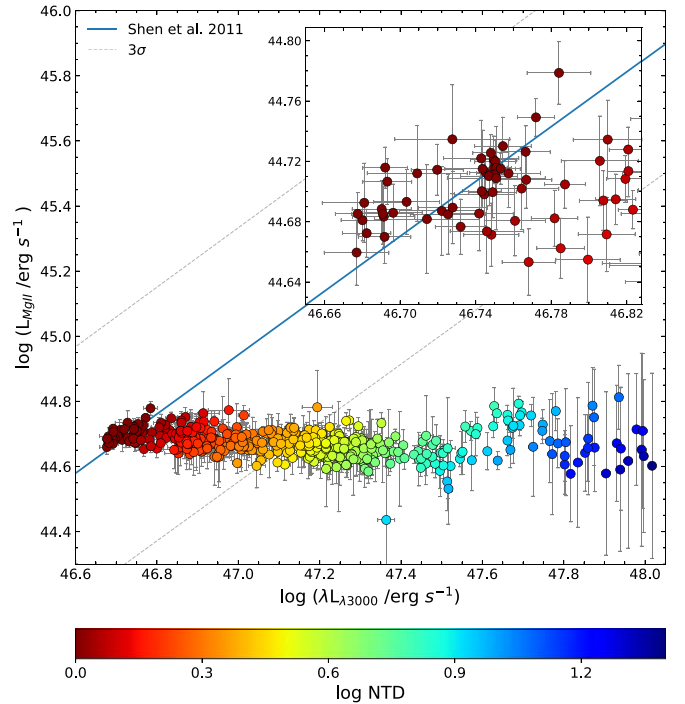


Figure 7. Variation of the Mg II $\lambda 2798$ emission-line luminosity with the $\lambda 3000$ continuum luminosity, for 3C 454.3 (our data). The color bar indicates for each observation the NTD value on a logarithmic scale, ranging from 0 to 1.4. Disk dominance applies between 0 and 0.3 while jet dominance begins after 0.3. The blue solid line and dashed lines represent the bisector fit and its uncertainty at 3σ , respectively, for a non-blazar sample of Shen et al. (2011). The inset is a closer look at the points near to the blue line; the NTD values of these points are below 0.3.

6.4. Implications for Calculation of the Black Hole Mass

In Figure 7 the relation between the luminosities of the $\lambda 3000$ continuum and the Mg II $\lambda 2798$ emission line of the observations is compared to the relation calculated by Shen et al. (2011) for a non-blazar sample. It is clear that the points do not seem to follow this relation, at least not after $\text{NTD} = 2$ (considering the 3σ of uncertainty). This indicates that the relation does not hold when the continuum is mainly nonthermal. The same behavior was seen for CTA 102 (Chavushyan et al. 2020). This illustrates the important fact that if the optical continuum of a strong radio-loud source is affected by the jet, then the luminosity of the $\lambda 3000$ continuum will be overestimated. In this case, we are seeing that BLR material close to the base of the jet (beyond the canonical BLR) is involved in the Mg II emission as well. The reverberation mapping (Blandford & McKee 1982; Peterson 1993) and single-epoch (e.g., Vestergaard & Peterson 2006) techniques for the calculation of the black hole mass depend crucially on having only a single source of ionization (the accretion disk) and the BLR clouds being in virial equilibrium. Neither of these conditions is fulfilled by 3C 454.3. We could take an average of the Mg II luminosity, which does not vary radically with the changes in the UV continuum, and apply the single-epoch technique (e.g., Wang et al. 2009). However, the ideal calculation should be performed by only taking the spectra for which the accretion disk is the dominant source of the continuum ($\text{NTD} < 2$), and then proceeding with either of the techniques.

7. Summary

Over the years, the blazar 3C 454.3 has been an object of interest due to its frequent periods of high activity. Now, we have been able to analyze the spectroscopic data (2009–2018) from the monitoring program of the ground-based observational support of the Fermi Gamma-ray Space Telescope at the University of Arizona. The redshift of this source ($z = 0.859$) unlocks the near-UV region of the spectrum, allowing us to analyze the Mg II $\lambda 2798$ emission line and the UV Fe II band, as well as to obtain the $\lambda 3000$ continuum. Besides this, we obtained multiple different wave bands from public sources to analyze their respective variability and find the role they play in the flaring events that occurred in 2010 and 2014. The most important results found in this work are listed below.

1. The brightest flares of 2010 and 2014 caused by the ejection of a blob (B11 and K14, respectively) from the 43 GHz core were also observed in the multiple wavelengths discussed in this work. The quasi-stationary component C presented a flaring event after the major flare of 2014 coinciding within the uncertainty with our estimated time of collision between the blob B11 and the quasi-stationary component C. This is an indication that the second flaring period was a superposition of multiple events at different locations.
2. The amplitude of the 15 GHz emission is comparable in the two flaring periods. Meanwhile, the 1 mm flux had a smaller increase during the second flaring period than during the first. The spectral index, within these frequencies, had faster changes during the first flaring period than during the second. This indicates that the physical conditions and/or processes during these periods were different. We suggest that the strange behavior of the spectral index is a result of a superposition of multiple events at different locations.
3. The cross-correlation results show that the emission of the seed photons has a small time lag (of a few days) against the synchrotron emission during the first flaring period. For the second period, the resultant delay is consistent with zero, meaning that the seed photons are coming from the same region as the synchrotron emission itself. To confirm the nature of each individual flare during the second flaring period, a SED study using multizone modeling needs to be performed.
4. The Mg II and Fe II behave differently from each other. The Mg II has an anticorrelation with the continuum while Fe II correlates positively, except by the time of the brightest flare of 2010, when both have a strong response at high continuum luminosities. However, Fe II showed the strongest response. This disparate behavior might be interpreted as BLR clouds comprising different zones or might simply be because of the different radiative properties of these elements.
5. The Mg II and Fe II behave differently during the two flaring periods. In the first flaring period, the emission lines do not behave monotonically with the increasing continuum. After the threshold that was found, both increase their luminosities in correlation with the continuum luminosity. However, during the second flaring period (and at low luminosities of the first flaring

period) the Mg II presents a weak anticorrelation while Fe II seems to respond positively to the increasing continuum. This might be explained by the difference in the ionizing spectrum, the state and availability of the BLR, or a different location of the BLR clouds during the second flaring period.

The ionizing continuum for almost the whole light curve is dominated by the nonthermal emission, and the Mg II emission is likely to be coming from two different regions: the BLR material inside the inner parsec and the material related to the jet near the 43 GHz core at ~ 9 pc from the black hole. Therefore, for reverberation mapping and single-epoch techniques to estimate the black hole mass, we strongly recommend using only data for which the accretion disk is the dominant source of continuum ($\text{NTD} < 2$), otherwise the errors might be large. For this particular case, the observations with $\text{NTD} < 2$ represent 35% of all the data.

In the future, we will continue performing multiwavelength studies and analyzing the spectral features of different blazar-type AGNs to further investigate the presence of BLR material beyond the inner parsec of the central engine. Studies of this type represent an important tool to find clues about the dominant gamma-ray emission mechanism. It is of particular importance to continue these studies since the determination of the dominant gamma-ray emission mechanism seems to be more complicated than thought before. Such a determination could break the dichotomy of the dominant emission mechanism for FSRQs and BL Lacs.

We thank the anonymous referee for the constructive comments that helped to improve the manuscript. This work was supported by CONACyT (Consejo Nacional de Ciencia y Tecnología) research grant 280789 (Mexico). R.A.A.-A. acknowledges support from the CONACyT program for PhD studies. This work is supported by the MPIR-Mexico Max Planck Partner Group led by V.M.P.-A. Data from the Steward Observatory spectropolarimetric monitoring project were used. This program is supported by Fermi Guest Investigator grants NNX08AW56G, NNX09AU10G, NNX12AO93G, and NNX15AU81G. This paper has made use of up-to-date SMARTS optical/near-infrared light curves that are available at www.astro.yale.edu/smarts/glast/home.php. The 1 mm flux density light curve data from the Submillimeter Array were provided by Mark A. Gurwell. The Submillimeter Array is a joint project between the Smithsonian Astrophysical Observatory and the Academia Sinica Institute of Astronomy and Astrophysics and is funded by the Smithsonian Institution and the Academia Sinica. This research has made use of data from the OVRO 40 m monitoring program (Richards et al. 2011), which is supported in part by NASA grants NNX08AW31G, NNX11A043G, and NNX14AQ89G and NSF grants AST-0808050 and AST-1109911.

Software: IRAF (Tody 1986, 1993), FTOOLS (Blackburn 1995), XSPEC (Arnaud 1996), Fermitools (v 1.0.20), SciPy (Virtanen et al. 2020)

Appendix A Cross-correlation Analysis Figures

Cross-correlations are shown in Figures 8–10.

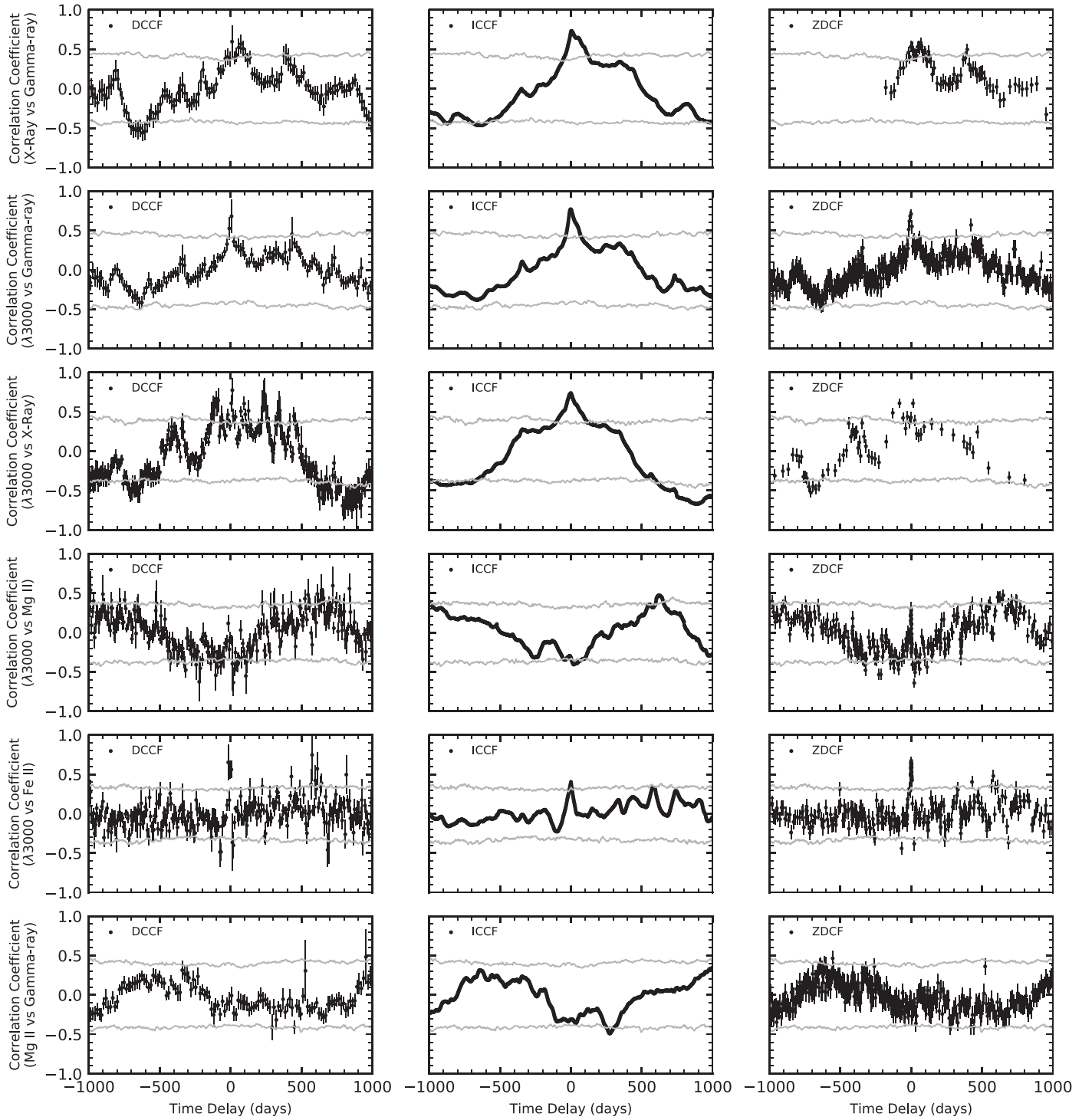


Figure 8. Cross-correlations for the complete data set (see Section 3.1). The complete figure set (six images) is available in the online journal. Each row corresponds to an analysis done for the two respective features using three different methods. The first method is the discrete cross-correlation function (DCCF), the second is the interpolation method (ICCF), and the third is the Z-transformed cross-correlation function (ZDCF). The significance at the 99% level is represented by a gray plot. The time delays that were found not to be aliases are listed in Table 2.

(The complete figure set (6 images) is available.)

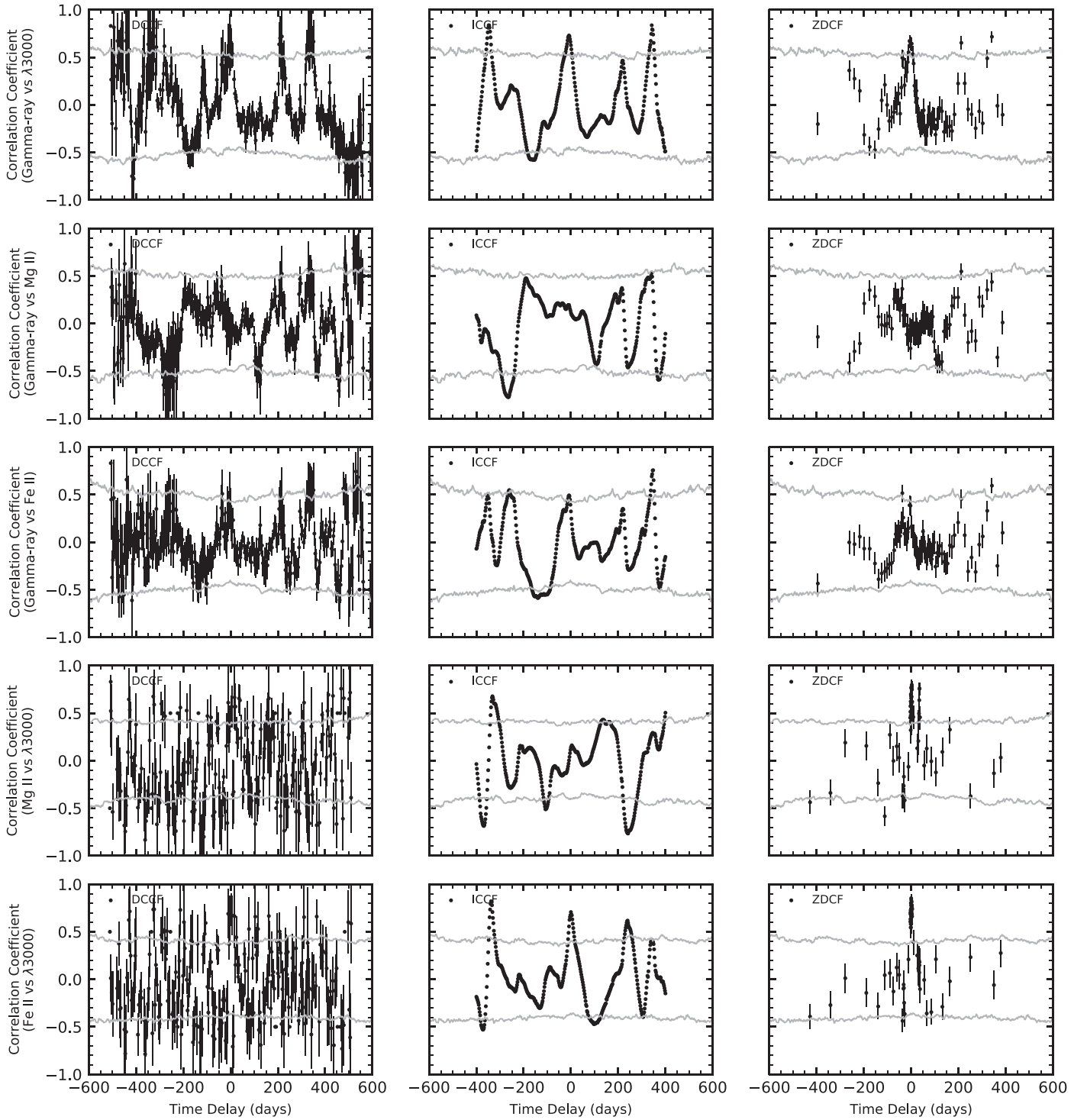


Figure 9. Cross-correlations for FP1 (see Section 3.2). The complete figure set of FP1 (two images) is available in the online journal. Each row corresponds to an analysis done for the two respective features using three different methods. The first method is the discrete cross-correlation function (DCCF), the second is the interpolation method (ICCF), and the third is the Z-transformed cross-correlation function (ZDCF). The significance at the 99% level is represented by a gray plot. The time delays that were found not to be aliases are listed in Table 3.

(The complete figure set (2 images) is available.)

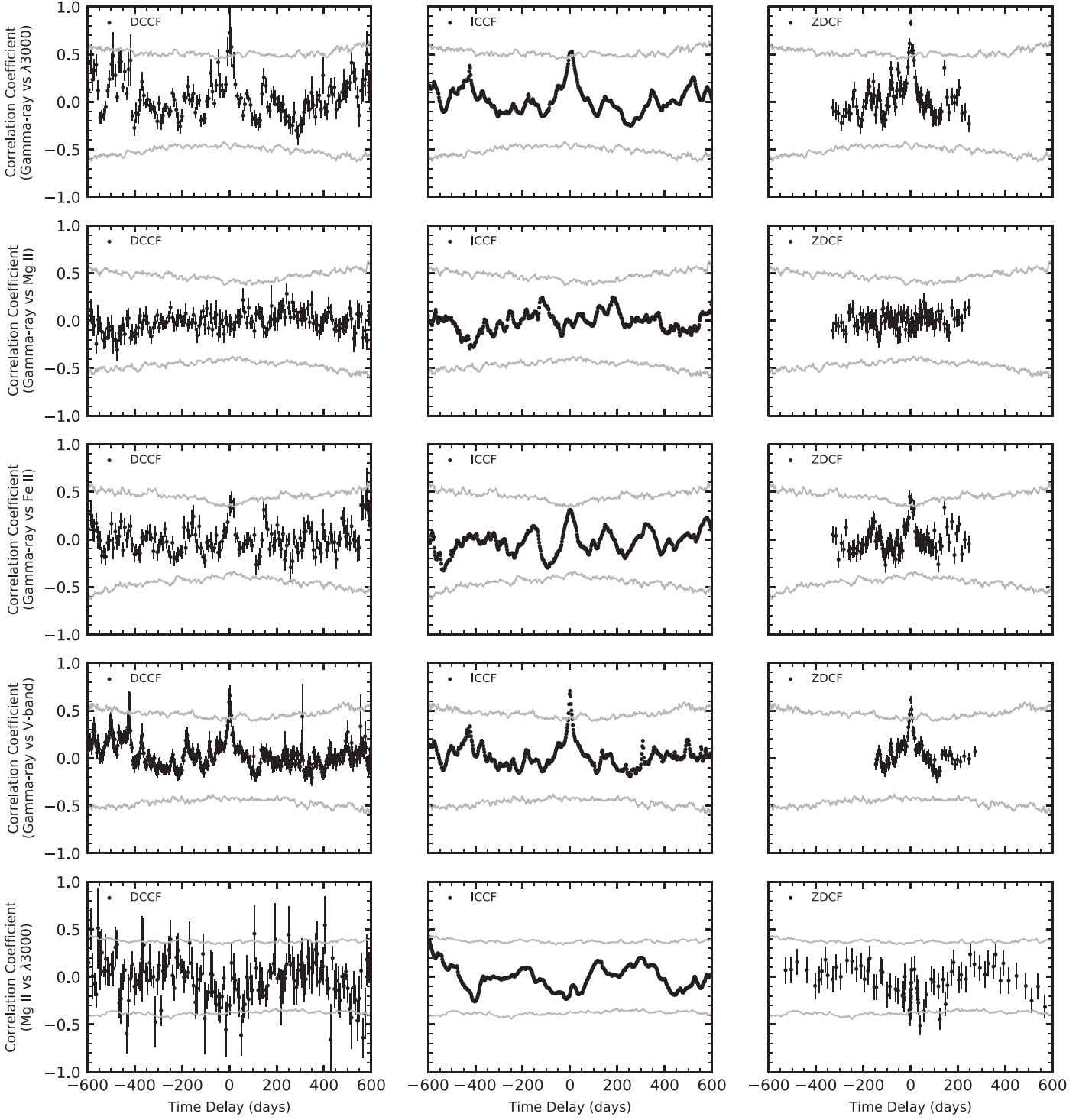





Figure 10. Cross-correlations for FP2 (see Section 3.2). The complete figure set of FP2 (two images) is available in the online journal. Each row corresponds to an analysis done for the two respective features using three different methods. The first method is the discrete cross-correlation function (DCCF), the second is the interpolation method (ICCF), and the third is the Z-transformed cross-correlation function (ZDCF). The significance at the 99% level is represented by a gray plot. The time delays that were found not to be aliases are listed in Table 3.

(The complete figure set (2 images) is available.)

ORCID iDs

Raúl A. Amaya-Almazán  <https://orcid.org/0000-0002-9443-7523>
 Vahram Chavushyan  <https://orcid.org/0000-0002-2558-0967>
 Victor M. Patiño-Álvarez  <https://orcid.org/0000-0002-5442-818X>

References

- Abdo, A. A., Ackermann, M., Ajello, M., et al. 2009, *APh*, **32**, 193
- Alexander, T. 1997, in *Astrophysics and Space Science Library*, Vol. 218, *Astronomical Time Series*, ed. D. Maoz, A. Sternberg, & E. M. Leibowitz (Dordrecht: Kluwer), 163
- Angione, R. J. 1968, *PASP*, **80**, 339
- Arnaud, K. A. 1996, in *ASP Conf. Ser. 101, XSPEC: The First Ten Years*, ed. G. H. Jacoby & J. Barnes (San Francisco, CA: ASP), 17
- Arshakian, T. G., León-Tavares, J., Lobanov, A. P., et al. 2010, *MNRAS*, **401**, 1231
- Arshakian, T. G., Lobanov, A. P., Chavushyan, V. H., et al. 2012, *A&AT*, **27**, 425
- Baldwin, J. A., Ferland, G. J., Korista, K. T., Hamann, F., & LaCluyzé, A. 2004, *ApJ*, **615**, 610
- Blackburn, J. K. 1995, in *ASP Conf. Ser. 77, FTOOLS: A FITS Data Processing and Analysis Software Package*, ed. R. A. Shaw, H. E. Payne, & J. J. E. Hayes (San Francisco, CA: ASP)
- Blandford, R. D., & McKee, C. F. 1982, *ApJ*, **255**, 419
- Blinov, D., Pavlidou, V., Papadakis, I., et al. 2018, *MNRAS*, **474**, 1296
- Bloom, S. D., & Marscher, A. P. 1996, *ApJ*, **461**, 657
- Bonning, E., Urry, C. M., Bailyn, C., et al. 2012, *ApJ*, **756**, 13
- Bosch-Ramon, V., Peruchó, M., & Barkov, M. V. 2012, *A&A*, **539**, A69
- Böttcher, M. 2007, *Ap&SS*, **309**, 95
- Böttcher, M., & Dermer, C. D. 1998, *ApJL*, **501**, L51
- Böttcher, M., Reimer, A., Sweeney, K., & Prakash, A. 2013, *ApJ*, **768**, 54
- Britto, R. J., Bottacini, E., Lott, B., Razzaque, S., & Buson, S. 2016, *ApJ*, **830**, 162
- Chandra, S., Zhang, H., Kushwaha, P., et al. 2015, *ApJ*, **809**, 130
- Chavushyan, V., Patiño-Álvarez, V. M., Amaya-Almazán, R. A., & Carrasco, L. 2020, *ApJ*, **891**, 68
- Chen, X., Fossati, G., Böttcher, M., & Liang, E. 2012, *MNRAS*, **424**, 789
- Coogan, R. T., Brown, A. M., & Chadwick, P. M. 2016, *MNRAS*, **458**, 354
- Daly, R. A., & Marscher, A. P. 1988, *ApJ*, **334**, 539
- Das, A. K., Prince, R., & Gupta, N. 2020, *ApJS*, **248**, 8
- Dietrich, M., Hamann, F., Appenzeller, I., & Vestergaard, M. 2003, *ApJ*, **596**, 817
- Fan, J. H., Tao, J., Liu, Y., et al. 2018, *AJ*, **155**, 90
- Finke, J. D., & Dermer, C. D. 2010, *ApJL*, **714**, L303
- Fromm, C. M., Peruchó, M., Ros, E., et al. 2011, *A&A*, **531**, A95
- Ghisellini, G., & Madau, P. 1996, *MNRAS*, **280**, 67
- Ghisellini, G., Tavecchio, F., & Chiaberge, M. 2005, *A&A*, **432**, 401
- Gupta, A. 2018, *Galax*, **6**, 1
- Gurwell, M. A., Peck, A. B., Hostler, S. R., Darrah, M. R., & Katz, C. A. 2007, in *ASP Conf. Ser. 375, From Z-Machines to ALMA: (Sub)Millimeter Spectroscopy of Galaxies*, ed. A. J. Baker et al. (San Francisco, CA: ASP), 234
- Hu, W., Fan, Z.-H., & Dai, B.-Z. 2015, *RAA*, **15**, 1455
- Hughes, P. A., Aller, M. F., & Aller, H. D. 2011, *ApJ*, **735**, 81
- Isler, J. C., Urry, C. M., Coppi, P., et al. 2013, *ApJ*, **779**, 100
- Itoh, R., Fukazawa, Y., Tanaka, Y. T., et al. 2013, *ApJL*, **768**, L24
- Janiak, M., Sikora, M., Nalewajko, K., Moderski, R., & Madejski, G. M. 2012, *ApJ*, **760**, 129
- Jorstad, S. G., Marscher, A. P., Larionov, V. M., et al. 2010, *ApJ*, **715**, 362
- Jorstad, S. G., Marscher, A. P., Morozova, D. A., et al. 2017, *ApJ*, **846**, 98
- Jorstad, S. G., Marscher, A. P., Smith, P. S., et al. 2013, *ApJ*, **773**, 147
- Kaspi, S., Maoz, D., Netzer, H., et al. 2005, *ApJ*, **629**, 61
- Kemball, A. J., Diamond, P. J., & Pauliny-Toth, I. I. K. 1996, *ApJL*, **464**, L55
- Khangulyan, D. V., Barkov, M. V., Bosch-Ramon, V., Aharonian, F. A., & Dorodnitsyn, A. V. 2013, *ApJ*, **774**, 113
- Kushwaha, P., Gupta, A. C., Misra, R., & Singh, K. P. 2016, *MNRAS*, **464**, 2046
- Kutkin, A. M., Sokolovsky, K. V., Lisakov, M. M., et al. 2014, *MNRAS*, **437**, 3396
- Laing, R. A. 1980, *MNRAS*, **193**, 439
- León-Tavares, J., Chavushyan, V., Lobanov, A., Valtaoja, E., & Arshakian, T. G. 2015, in *IAU Symp. 313, Extragalactic Jets from Every Angle*, ed. F. Massaro et al. (Cambridge: Cambridge Univ. Press), 43
- León-Tavares, J., Chavushyan, V., Patiño-Álvarez, V., et al. 2013, *ApJL*, **763**, L36
- León-Tavares, J., Lobanov, A. P., Chavushyan, V. H., et al. 2010, *ApJ*, **715**, 355
- Liodakis, I., Blinov, D., Jorstad, S. G., et al. 2020, *ApJ*, **902**, 61
- Marscher, A. P. 2014, *ApJ*, **780**, 87
- Marscher, A. P., & Gear, W. K. 1985, *ApJ*, **298**, 114
- Marscher, A. P., Jorstad, S. G., D'Arcangelo, F. D., et al. 2008, *Natur*, **452**, 966
- Marscher, A. P., Jorstad, S. G., Larionov, V. M., et al. 2010, *ApJL*, **710**, L126
- Nalewajko, K., Gupta, A. C., Liao, M., et al. 2019, *A&A*, **631**, A4
- Paltani, S., & Türler, M. 2003, *ApJ*, **583**, 659
- Park, J., Lee, S.-S., Kim, J.-Y., et al. 2019, *ApJ*, **877**, 106
- Park, J.-H., & Trippie, S. 2014, *ApJ*, **785**, 76
- Patiño-Álvarez, V. M., Dzib, S. A., Lobanov, A., & Chavushyan, V. 2019, *A&A*, **630**, A56
- Patiño-Álvarez, V. M., Fernandes, S., Chavushyan, V., et al. 2018, *MNRAS*, **479**, 2037
- Patiño-Álvarez, V. M., Torrealba, J., Chavushyan, V., et al. 2016, *FrASS*, **3**, 19
- Pauliny-Toth, I. I. K., Porcas, R. W., Zensus, J. A., et al. 1987, *Natur*, **328**, 778
- Peirson, A. L., & Romani, R. W. 2018, *ApJ*, **864**, 140
- Peirson, A. L., & Romani, R. W. 2019, *ApJ*, **885**, 76
- Perez, E., Penston, M. V., & Moles, M. 1989, *MNRAS*, **239**, 75
- Peterson, B. M. 1993, *PASP*, **105**, 247
- Peterson, B. M. 1997, *An Introduction to Active Galactic Nuclei* (Cambridge: Cambridge Univ. Press)
- Poutanen, J., & Stern, B. 2010, *ApJL*, **717**, L118
- Press, W. H., Teukolsky, S. A., Vetterling, W. T., & Flannery, B. P. 2007, *Numerical Recipes 3rd Edition: The Art of Scientific Computing* (3rd edn.; Cambridge: Cambridge Univ. Press), <https://www.cambridge.org/numericalrecipes>
- Rajput, B., Stalin, C. S., Sahayanathan, S., Rakshit, S., & Mandal, A. K. 2019, *MNRAS*, **486**, 1781
- Richards, J. L., Max-Moerbeck, W., Pavlidou, V., et al. 2011, arXiv:1111.0318
- Romero, G. E., Boettcher, M., Markoff, S., & Tavecchio, F. 2017, *SSRv*, **207**, 5
- Sarkar, A., Chitnis, V. R., Gupta, A. C., et al. 2019, *ApJ*, **887**, 185
- Shah, Z., Sahayanathan, S., Mankuzhiyil, N., et al. 2017, *MNRAS*, **470**, 3283
- Shaw, M. S., Romani, R. W., Cotter, G., et al. 2012, *ApJ*, **748**, 49
- Shen, Y., Richards, G. T., Strauss, M. A., et al. 2011, *ApJS*, **194**, 45
- Sher, D. 1968, *JRASC*, **62**, 105
- Sikora, M., Begelman, M. C., & Rees, M. J. 1994, *ApJ*, **421**, 153
- Sikora, M., Moderski, R., & Madejski, G. M. 2008, *ApJ*, **675**, 71
- Sikora, M., Rutkowski, M., & Begelman, M. C. 2016, *MNRAS*, **457**, 1352
- Smith, P. S., Montiel, E., Rightley, S., et al. 2009, arXiv:0912.3621
- Stroh, M. C., & Falcone, A. D. 2013, *ApJS*, **207**, 28
- Tavani, M., Vittorini, V., & Cavaliere, A. 2015, *ApJ*, **814**, 51
- Tavecchio, F., Ghisellini, G., Bonnoli, G., & Ghirlanda, G. 2010, *MNRAS*, **405**, L94
- The Fermi-LAT collaboration 2020, *ApJS*, **247**, 33
- Tody, D. 1986, *Proc. SPIE*, **627**, 733
- Tody, D. 1993, in *ASP Conf. Ser. 52, IRAF in the Nineties*, ed. R. J. Hanisch et al. (San Francisco, CA: ASP)
- Tornikoski, M., Valtaoja, E., Terasranta, H., et al. 1994, *A&A*, **289**, 673
- Tresse, L., Maddox, S., Loveday, J., & Singleton, C. 1999, *MNRAS*, **310**, 262
- Trippie, S., Krips, M., Piétu, V., et al. 2011, *A&A*, **533**, A97
- Urry, C. M., & Padovani, P. 1995, *PASP*, **107**, 803
- Valtaoja, E., Terasranta, H., Urpo, S., et al. 1992, *A&A*, **254**, 71
- Verner, E., Bruhweiler, F., Verner, D., Johansson, S., & Gull, T. 2003, *ApJL*, **592**, L59
- Verner, E. M., Verner, D. A., Korista, K. T., et al. 1999, *ApJS*, **120**, 101
- Vestergaard, M., & Peterson, B. M. 2006, *ApJ*, **641**, 689
- Vestergaard, M., & Wilkes, B. J. 2001, *ApJS*, **134**, 1
- Virtanen, P., Gommers, R., Oliphant, T. E., et al. 2020, *NatMe*, **17**, 261
- Vittorini, V., Tavani, M., Cavaliere, A., Striani, E., & Vercellone, S. 2014, *ApJ*, **793**, 98
- Wang, J.-G., Dong, X.-B., Wang, T.-G., et al. 2009, *ApJ*, **707**, 1334
- Weaver, Z. R., Balonek, T. J., Jorstad, S. G., et al. 2019, *ApJ*, **875**, 15
- Wills, B. J., Netzer, H., & Wills, D. 1985, *ApJ*, **288**, 94
- Zacharias, M., Böttcher, M., Jankowsky, F., et al. 2019, *ApJ*, **871**, 19
- Zacharias, M., & Schlickeiser, R. 2012, *ApJ*, **761**, 110
- Zhang, H. 2019, *Galax*, **7**, 85
- Zhang, H.-M., Wang, Z.-J., Zhang, J., et al. 2020, *PASJ*, **72**, 44
- Zhang, H.-M., Zhang, J., Lu, R.-J., et al. 2018, *RAA*, **18**, 040
- Zhang, L. X., & Fan, J. H. 2018, *Ap&SS*, **363**, 142